



Modeling of pseudoelasticity via reversible slip in Fe₃Ga



J. Wang, H. Sehitoglu*

Department of Mechanical Science and Engineering, University of Illinois at Urbana–Champaign, 1206 W. Green St., Urbana, IL 61801, USA

ARTICLE INFO

Article history:

Received 18 November 2013

Received in revised form 31 January 2014

Accepted 2 February 2014

Available online 25 February 2014

Keywords:

Pseudoelasticity

Critical stress

Density Functional Theory

APB

Reversible slip

ABSTRACT

The Fe₃Ga alloy with the cubic D0₃ lattice possesses considerable recoverable strain due to the slip reversibility. Pseudoelasticity via reversible slip in Fe₃Ga is studied with atomistic simulations. An extended Peierls–Nabarro model incorporating the Generalized Stacking Fault Energy (GSFE) is established to determine Peierls stress in D0₃ and L1₂ Fe₃Ga. The back stress and frictional stress are predicted during loading and unloading process. These stress magnitudes govern the reversible slip in Fe₃Ga. The results show that the reversible slip observed experimentally in D0₃ Fe₃Ga is induced by its larger back stress compared to its frictional stress. In contrast, the reversible slip cannot appear in L1₂ since its back stress is not large enough to pull back superpartials, and thus the existence of L1₂ will suppress the pseudoelasticity of D0₃ Fe₃Ga and results in decreasing the strain recovery. The present study has explored the theoretical foundations of this phenomenon arising from high back stresses responsible for cyclic reversible dislocation motion.

© 2014 Elsevier B.V. All rights reserved.

1. Introduction

Pseudoelasticity remains an intriguing topic in materials science [1–6] and mechanics of materials [7–11]. It refers to the deformation of the material in the nonlinear regime and recovery of the deformation upon removal of the load. It involves strains well beyond the classical elastic strains, and can occur where the martensite phase reverts back to austenite, or when twin or slip boundaries move back to their original configuration upon removal of the load. In the present study, the term ‘slip boundaries’ is used interchangeably with ‘antiphase boundaries (APBs)’ pulling back the superpartials, which results in pseudoelasticity. The reversible phase transformation is characteristic of shape memory alloys (SMAs) [12] and has attracted considerable attention. The twinning and detwinning processes [13] can also occur in shape memory alloys where the domain boundaries translate, and this adds to the shape memory strains. It is known but not well understood. The phenomenon for pseudoelasticity under to- and fro-motion of dislocations is not well known and not well understood. It has been demonstrated experimentally in Fe–Ga and Fe–Al alloys [14–16]. The requirement of single slip system activation and sufficient back stresses are two factors that facilitate the reversible slip motion in these ordered alloys. If cross slip occurs or interactions with conjugate systems develops this can curtail recoverability. Experimental observations show that reversible slip can occur in Fe₃Al and Fe₃Ga alloys due to the dislocation motion within the

antiphase boundaries (APB) [14,16–22] (Fig. 1). The APB in ordered alloys is a planar defect of a crystal where atoms are configured in an opposite order compared to the perfect crystal. The energy barriers for dislocation motion within the APB (the APB energy) can be determined from atomistic simulations. Then, the motion of a group of dislocations are influenced by the neighboring dislocations on the same plane. This requires a mesoscale formulation of the forces and overall energy. The purpose of this paper is to propose a mesoscale model incorporating back stresses responsible for cyclic reversible dislocation motion.

There are two types of APBs in the D0₃ superlattice: the nearest-neighbor APB (NNAPB) and the next-nearest-neighbor APB (NNNAPB). The NNAPB is formed by the dislocation slip $\frac{1}{4}\langle 111 \rangle\{110\}$ and has wrong first nearest-neighbor bonds of Ga–Ga. While, the NNNAPB is formed by a dislocation slip $\frac{1}{2}\langle 111 \rangle\{110\}$ and has wrong next-nearest-neighbor bonds of Ga–Ga.

It has been reported that single crystals of Fe₃Ga with the cubic D0₃ structure exhibit pseudoelasticity of several percent strain and these recoverable strains are comparable to NiTi alloys [21]. The reversible slip in Fe₃Ga and Fe₃Al can occur over a broader range of temperature [21–24]. This is in contrast to the pseudoelasticity based on phase transformation, which appears above the austenite finish temperature A_f [25,26] over a narrow temperature regime of the order of 15 °C. Therefore, it is very important to understand the mechanism of APB pseudoelasticity in metallic alloys and lay the foundation to potentially exploit this phenomenon.

The APB pseudoelasticity in the single crystal of D0₃ Fe₃Ga is shown in Fig. 1. The slip on the $\{110\}\langle 111 \rangle$ system and the crystal structure are shown in Fig. 2 [14,15,20]. Fig. 2a shows the $\{110\}$

* Corresponding author. Tel.: +1 217 333 4112; fax: +1 217 244 6534.

E-mail address: huseyin@illinois.edu (H. Sehitoglu).

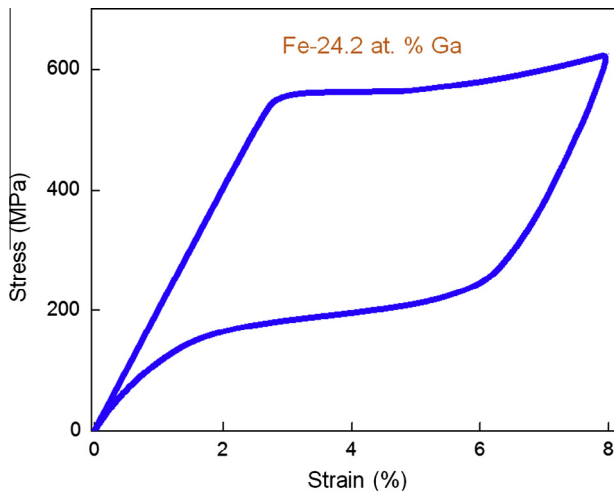


Fig. 1. The APB pseudoelasticity in Fe_3Ga (from Ref. [21]). Dislocation slip reversibility upon loading and unloading results in reversible behavior. The material remains in the D0_3 phase and there is no martensitic phase transformation.

slip plane and the $\langle 111 \rangle$ slip direction in the unit cell of the austenite $\text{D0}_3 \text{Fe}_3\text{Ga}$. We note that the lattice parameter a_0 represents repeating atom positions in $\langle 100 \rangle$ directions, and the D0_3 unit cell contains eight B2 type subcells. In each subcell the Fe atoms occupy corners and since there are eight subcells, the corner atoms provide eight Fe atoms in the D0_3 unit cell. Additionally, four Fe atoms occupy the centers of four subcells, and four Ga atoms occupy the centers of other four subcells. Thus, the total number of atoms in the D0_3 unit cell is sixteen and the atom ratio of Fe to Ga is 3:1. Upon shearing in the $\langle 111 \rangle$ direction, the dissociation of the $\langle 111 \rangle$ superlattice dislocation into four $\frac{1}{4}\langle 111 \rangle$ superpartials associated with the NNAPB and the NNNAPB is noted. Upon unloading, the NNAPB and NNNAPB pull back uncoupled $\frac{1}{4}\langle 111 \rangle$ superpartials (mode 1) and paired $\frac{1}{4}\langle 111 \rangle$ superpartials (mode 2) shown in Fig. 2b, which results in APB pseudoelasticity. Even though the APB pseudoelasticity is very important in $\text{D0}_3 \text{Fe}_3\text{Ga}$, a quantitative formulation for this mechanism is still lacking, especially the determination of stacking fault energies NNAPB and NNNAPB. In the present work, we address the atomistic mechanism of slip reversibility by establishing the Generalized Stacking Fault Energy (GSFE) curve in slip system $\{110\}\langle 111 \rangle$. We calculate shear stresses associated to the APB pseudoelasticity under loading and unloading and compare with available experimental measurements.

From the Fe–Ga alloy phase equilibrium diagram we note that the D0_3 single phase region forms around 600°C while L1_2 can develop below 600°C . The formation of L1_2 may affect the APB pseudoelasticity of $\text{D0}_3 \text{Fe}_3\text{Ga}$ [27]. Thus, it is important to theoretically study the slip behavior of $\text{L1}_2 \text{Fe}_3\text{Ga}$ by determining its GSFE

curve and comparing with D0_3 structure, and then understand the effect of formation of L1_2 on APB pseudoelasticity in Fe–Ga alloys. Since with D0_3 structure of Fe_3Ga , APB pseudoelasticity will extend the shape memory capabilities and defy the classical notions of SMAs [14]. We focus on establishing the atomic movements and the energy landscapes to develop a general methodology for understanding the SMAs with reversible dislocation slip, and finally calculate shear stresses associated with slip and compare the results with experiments.

2. Simulations

The first-principles calculations based on the Density Functional Theory (DFT) were carried out to calculate the systems total-energy [28]. In this study, we utilized the Vienna ab initio Simulations Package (VASP) with the projector augmented wave (PAW) method and the generalized gradient approximation (GGA) as implementations of DFT [29,30]. In our calculations, we used a $9 \times 9 \times 9$ Monkhorst Pack k -point meshes for the Brillouion-zone integration to ensure the convergence of results. Ionic relaxation was performed by a conjugate gradient algorithm and stopped when absolute values of internal forces were smaller than $5 \times 10^{-3} \text{ eV}/\text{\AA}$. The energy cut-off of 500 eV was used for the plane-wave basis set. The total energy was converged to less than 10^{-5} eV per atom. For GSFE calculations a full internal atom relaxation, including perpendicular and parallel directions to the fault plane, was allowed for minimizing the short-range interaction between misfitted layers near to the fault plane. This relaxation process caused a small additional atomic displacement r ($|r| = \sqrt{r_x^2 + r_y^2 + r_z^2}$). Thus, the total fault displacement is not exactly equal to the applied shear displacement, u , but involves additional r . The total energy of the deformed (faulted) crystal was minimized during this relaxation process through which atoms can avoid coming too close to each other during shear [31–34].

2.1. Lattice parameters and energies of D0_3 and $\text{L1}_2 \text{Fe}_3\text{Ga}$

We calculated the crystal structural energy variation with lattice parameters of D0_3 (Fig. 3a) and L1_2 (Fig. 3b) Fe_3Ga . The lattice parameters correspond to the lowest structural energy levels. The results are given in Table 1 and in an excellent agreement with experiments. These precisely obtained lattice parameters form the foundation of first-principles calculations in this study. In Table 1 the slip system and calculated Burgers vector are also given.

2.2. Dislocation slip (GSFE) in $\text{D0}_3 \text{Fe}_3\text{Ga}$

The energy barrier during dislocation motion in a glide system is measured in terms of the Generalized Stacking Fault Energy (GSFE) [38]. Also referred to as the fault energy curve, GSFE is

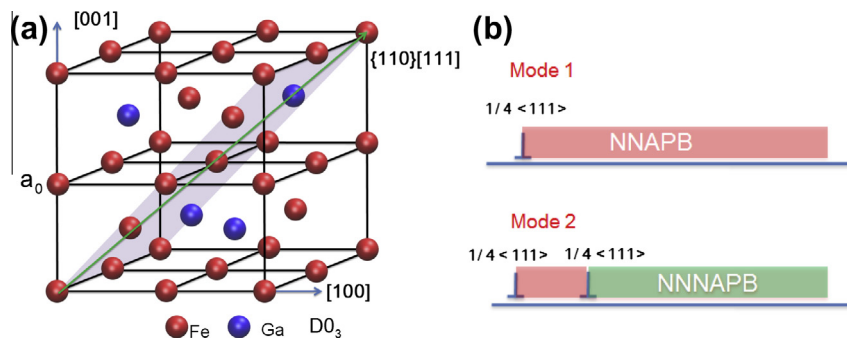


Fig. 2. (a) Schematic illustration of the $\{110\}$ slip plane (violet) and the $\langle 111 \rangle$ slip direction (green arrow) in the austenite D0_3 unit lattice of Fe_3Ga and (b) uncoupled and paired $\frac{1}{4}\langle 111 \rangle$ superpartials are pulled back by NNAPB (mode 1) and NNNAPB (mode 2), respectively. (For interpretation of the references to colour in this figure legend, the reader is referred to the web version of this article.)

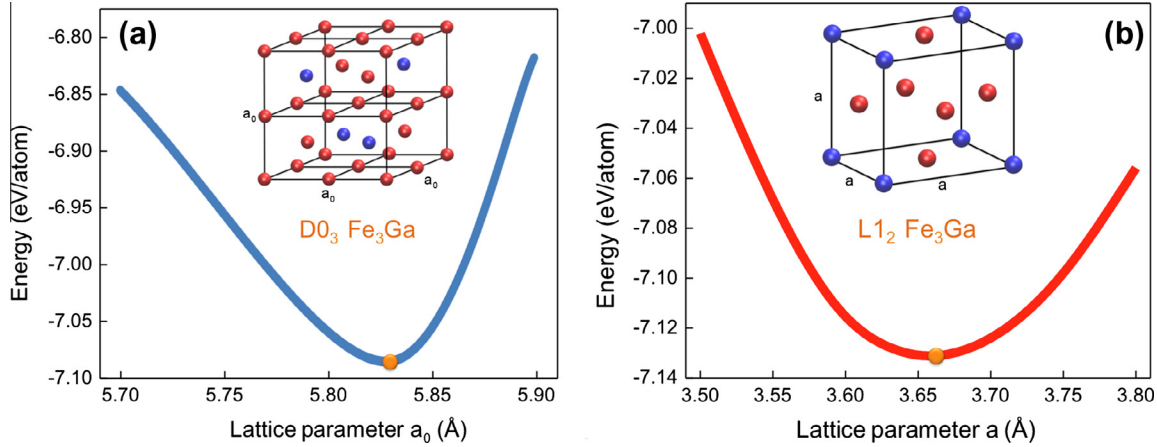


Fig. 3. Determination of lattice parameters for the $D0_3$ and $L1_2$ crystal structures of Fe_3Ga . (a) Structural energy variation with lattice parameter of $D0_3 Fe_3Ga$ and (b) structural energy variation with lattice parameter of $L1_2 Fe_3Ga$.

Table 1

Calculated lattice parameter and Burgers vector in $D0_3$ and $L1_2 Fe_3Ga$. The lattice parameter is compared to experiments.

| Fe_3Ga structures | Lattice parameter (Å) | | Slip system | Burgers vector (Å) |
|---------------------|-----------------------|--------------|-------------------------------------|--------------------|
| | This study | Experiments | | |
| $D0_3$ | 5.83 | 5.84 [35,36] | $\frac{1}{4}[111](\bar{1}01)$ | 2.52 |
| $L1_2$ | 3.66 | 3.67 [37] | $\frac{1}{6}[\bar{1}\bar{1}2](111)$ | 1.49 |

defined as the energy associated with a rigid shift of one elastic half crystal with respect to another half on a certain slip plane in a given slip direction [39]. During GSFE calculations, a complete landscape of fault energy is investigated which requires a displacement of a repeating unit lattice in the respective shear direction. We investigate the dislocation slip in the $(\bar{1}01)$ slip plane along $[111]$ slip direction consistent with experimental observations [20,21]. Fig. 4a shows a perfect lattice before shear viewed from the normal to the plane $(\bar{1}21)$, where the slip plane is shown as green dashed line. Fig. 4b is the lattice after shear by one-third Burgers vector $\frac{1}{3}b$ (red arrow). The Burgers vector $b = \frac{\sqrt{3}}{4}a_0$ is calculated as 2.52 Å, where $a_0 = 5.83$ Å is the $D0_3$ lattice parameter [35,40,41]. The different atom size represent the six successive $(\bar{1}21)$ layers from the top view. The largest atom represents in-plane and the atom size becomes smaller as the out-of-plane is displayed.

The calculated GSFE curve of the slip system $(\bar{1}01)[111]$ in $D0_3 Fe_3Ga$ is shown in Fig. 5. We note that the unstable stacking fault energy (energy barrier for dislocation movement) is near 210 mJ/m², and the nearest-neighbor APB (NNAPB) and the next-nearest-neighbor APB (NNNAPB) energies are $\gamma_{NN} = 34$ mJ/m² and $\gamma_{NNN} = 71$ mJ/m², respectively.

The superdislocation $[111]$ can dissociate into four superpartials $\frac{1}{4}[111]$ connected by the NNAPB (γ_{NN}) and NNNAPB (γ_{NNN}) energies as:

$$[111] = \frac{1}{4}[111] + NNAPB + \frac{1}{4}[111] + NNNAPB + \frac{1}{4}[111] + NNAPB + \frac{1}{4}[111] \quad (1)$$

The separations, d_1 and d_2 , of these four superpartials can be calculated using the force balance between attraction due to fault energies and elastic repulsion of partial dislocations [42,43]. The calculation detail is shown in Appendix A.

When APB pseudoelasticity occurs in $D0_3 Fe_3Ga$, the superpartials are pulled back by the APB tension, and the following equations should be satisfied during loading and unloading [16,21]:

$$\begin{aligned} \tau_p &= \tau_b + \tau_0 \\ \tau_b &= \tau_r + \tau_0 \end{aligned} \quad (2)$$

where τ_p is the Peierls stress (critical resolved shear stress) to move four superpartials; τ_b is the unidirectional back stress acting on the superpartial due to the APB surface tension; τ_0 is the bidirectional lattice frictional stress of a $\frac{1}{4}[111]$ superpartial, which can be considered as the Peierls stress to move a single superpartial; τ_r is the recovery-start shear stress, which is the critical stress for the backward motion [16,21,27]. The τ_b is calculated from the first of Eq. (2) and then τ_r is computed from the second of Eq. (2). Fig. 6 shows a schematic illustration of a APB pseudoelasticity stress-strain curve and the stresses (τ_p , τ_b , τ_0 and τ_r) acting on superpartials during loading and unloading processes and resulting in the APB pseudoelasticity. The recovery stress will occur in tension if assisted by large back stresses, otherwise the reversed stress of dislocation motion will occur in compression similar to cyclic plasticity of metals [44].

The Peierls stress τ_p is calculated as 320 MPa using a modified Peierls–Nabarro model accounting for the multiple dislocations, which is the maximum slope of the misfit energy derived from GSFE to the position of dislocation line. The calculation details for τ_p are given in Appendix B.

To calculate the lattice frictional stress, τ_0 , we consider the total energy associated with the $\frac{1}{4}[111]$ superpartial dislocation. This total energy, E_{total} , is composed of (1) elastic strain energy of dislocation itself (self-energy), E_s , (2) elastic strain energy due to the dislocations interaction (interaction energy), E_I , (3) the misfit energy associated with GSFE, E_γ , defined in Eq. (B1). Thus, the total energy associated with the $\frac{1}{4}[111]$ superpartial dislocation can be expressed as:

$$E_{total} = E_s + E_\gamma - E_I \quad (3)$$

Following the classical dislocation theory and treating the superpartials as a single dislocation pile-up, the elastic energies, E_s and E_I , can be written as [45,46]:

$$E_s = \frac{\mu b^2}{4\pi(1-\nu)}(1-\nu \cos^2 \theta) \ln \frac{L}{r_0} \quad (4)$$

$$E_I = \frac{\mu b^2}{4\pi(1-\nu)}(1-\nu \cos^2 \theta) \left(\ln \frac{L}{u-d_1} + \ln \frac{L}{u-(d_1+d_2)} + \ln \frac{L}{u-(2d_1+d_2)} \right) \quad (5)$$

where μ is the shear modulus in the slip system, b is the Burgers vector of the superpartial dislocations, ν is the Poisson's ratio, θ is

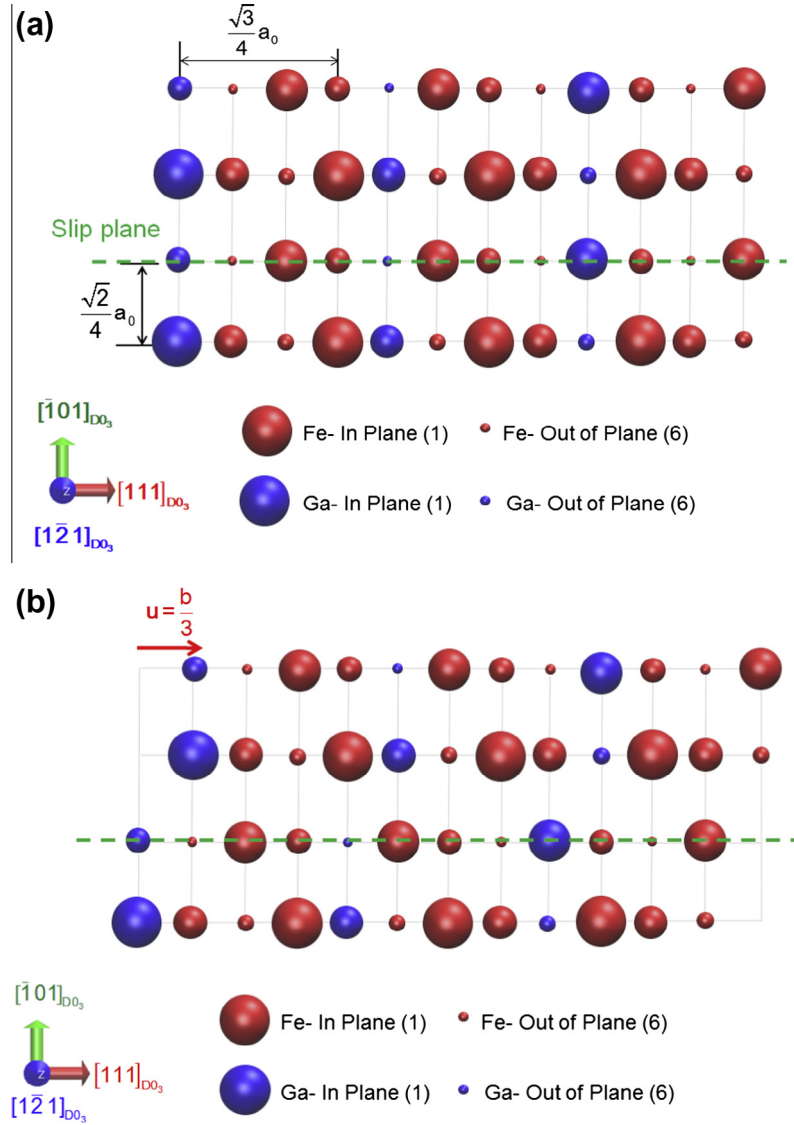


Fig. 4. Dislocation slip in the $(\bar{1}01)$ plane along $[111]$ slip direction. (a) The perfect $D0_3$ lattice observed from the $[\bar{1}\bar{2}1]$ direction. The slip plane $(\bar{1}01)$ is marked with a green dashed line. (b) The lattice after a rigid shear with displacement, $u = \frac{1}{3}b$ ($b = 2.51 \text{ \AA}$), shown in a red arrow. The different atom sizes represent the six successive $(\bar{1}\bar{2}1)$ layers from the top view. The largest atom represents in-plane and the atom sizes become smaller as the out-of-plane is displayed. (For interpretation of the references to colour in this figure legend, the reader is referred to the web version of this article.)

the angle between the Burgers vector and the dislocation line, L and r_0 are dimensions of the crystal containing the dislocations and inner cut-off radii, and u is the position of the dislocation line.

Having determined all energy terms in the total energy expression, the total energy of the $\frac{1}{4}[111]$ superpartial can be written as follows:

$$E_{\text{total}} = \frac{\mu b^2}{4\pi(1-\nu)}(1 - \nu \cos^2 \theta) \ln \frac{L}{r_0} + \sum_{m=-\infty}^{+\infty} \gamma(f(ma' - u))a' - \frac{\mu b^2}{4\pi(1-\nu)} \times (1 - \nu \cos^2 \theta) \left(\ln \frac{L}{u-d_1} + \ln \frac{L}{u-(d_1+d_2)} + \ln \frac{L}{u-(2d_1+d_2)} \right) \quad (6)$$

It can be seen that the total energy fluctuates as the position u changes, and this energy fluctuation is equivalent to an applied stress on the superpartial. Thus, the lattice frictional stress, τ_0 , can be obtained from the maximum derivative of the total energy E_{total} with respect to u , i.e.

$$\tau_0 = \frac{1}{b} \max \left(\frac{\partial E_{\text{total}}}{\partial u} \right) \quad (7)$$

The calculated τ_0 is 78 MPa, and from Eq. (2) the back stress τ_b and recovery-start stress τ_r are computed as 242 MPa and 164 MPa, respectively. We note that τ_r has the same sign with τ_p (both of them are tensile or compressive stresses) and τ_0 is smaller than τ_b , which satisfies the condition of APB pseudoelasticity [16,25].

2.3. Dislocation slip (GSFE) in $L1_2$ Fe_3Ga

It is experimentally observed that the $L1_2$ phase (fcc ordered alloy) can form below 600 °C in Fe–Ga alloys [27,47]. Here we investigate the slip system $\{111\}\langle 110 \rangle$ for $L1_2$ Fe_3Ga , which is often observed experimentally in $L1_2$ structures [48–51]. The $\langle 110 \rangle$ superdislocation in the $\{111\}$ slip plane can dissociate into two $\frac{1}{2}\langle 110 \rangle$ superpartials with formation of an APB energy. The two superpartials can further dissociate into two Shockley partials $\frac{1}{6}\langle 112 \rangle$ connected by CSF (complex stacking fault) energy [48–50,52–54]. This process results in a fourfold dissociation in Eq. (8):

$$[\bar{1}10] = \frac{1}{6}[\bar{2}11] + \text{CSF} + \frac{1}{6}[\bar{1}\bar{2}\bar{1}] + \text{APB} + \frac{1}{6}[\bar{2}11] + \text{CSF} + \frac{1}{6}[\bar{1}\bar{2}\bar{1}] \quad (8)$$

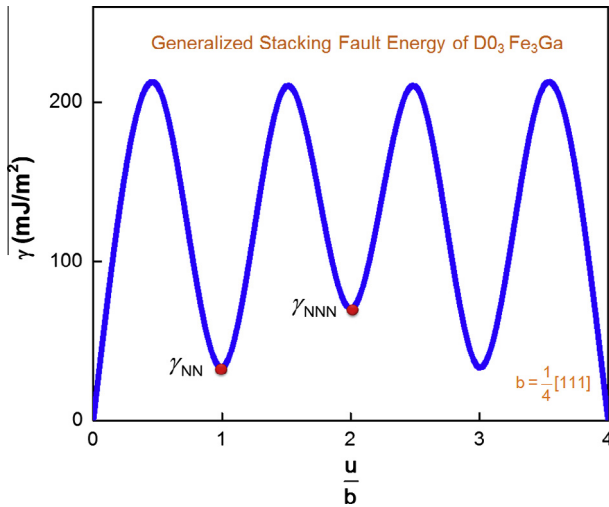


Fig. 5. GSFE curve corresponding to the slip system $(\bar{1}10)[111]$ in $D0_3$ Fe_3Ga . Upon shearing in the $[111]$ direction, the superdislocation $[111]$ dissociates into four superpartials $\frac{1}{4}[111]$ associated with NNAPB and NNNAPB energies. The unstable stacking fault energy is near 210 mJ/m^2 ; the NNAPB and the NNNAPB energies are 34 mJ/m^2 and 71 mJ/m^2 , respectively.

The planar defects CSF and APB in Eq. (8) are defined by pure movement of one half of a crystal over the other half in the (111) plane. This movement forms metastable positions possessing local minimum energies, which govern the dislocation slip behavior of $L1_2$ Fe_3Ga . Fig. 7 shows a top view from the direction perpendicular to the (111) slip plane with three-layer of atoms stacking in $L1_2$ Fe_3Ga . Three different sizes of atoms indicate three successive (111) layers from the top view and represent the atoms stacking sequence ...ABCABC..., which is similar to fcc metals. However, certain symmetries existing in fcc lattice are not found in $L1_2$ lattice. We note that $\{110\}$ planes composed of only Fe atoms (shown in brown dashed line in Fig. 7) are not planes of mirror-symmetry in the $L1_2$ lattice, which is different with the case of fcc lattice where every $\{110\}$ plane has this symmetry [55]. Therefore, the superdislocation $[\bar{1}10]$ (brown arrow) in $L1_2$ lattice must dissociate into four superpartials $\frac{1}{6}\langle 211 \rangle$ (green arrow) corresponding to Eq. (8). While in fcc lattice, the full dislocation $\frac{1}{2}[\bar{1}10]$ dissociates into two partials $\frac{1}{6}\langle 211 \rangle$ [56]. Two types of planar defects CSF and APB are formed with the dissociation of superdislocation $[\bar{1}10]$ in $L1_2$, which does not exhibit in fcc metals. A CSF is produced when the in-plane atoms and all atoms above are shifted along the Burgers vector $\frac{1}{6}\langle 211 \rangle$ ($a \rightarrow b$ and $c \rightarrow d$ in Fig. 7). An APB is formed when the in-plane atoms and all atoms

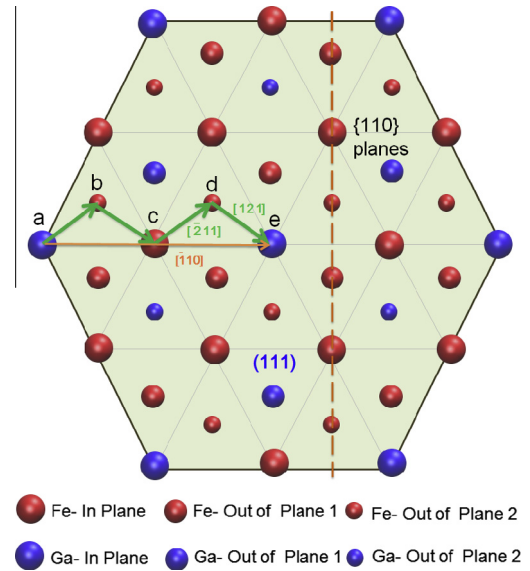


Fig. 7. Dislocations and atomic configurations of $L1_2$ Fe_3Ga in the (111) plane. Three different sizes of atoms represent three successive (111) layers from the top view. Dislocation $[\bar{1}10]$ can dissociate into four superpartials $\frac{1}{6}\langle 211 \rangle$ corresponding to Eq. (8). Two types of planar defects CSF ($a \rightarrow b$ and $c \rightarrow d$) and APB ($a \rightarrow c$ and $c \rightarrow e$) are formed. The points a, b, c, d and e correspond to the stable (metastable) positions of GSFE curve described later. The $\{110\}$ planes composed of only Fe atoms (shown in brown dashed line) are not planes of mirror-symmetry in the $L1_2$ lattice. (For interpretation of the references to colour in this figure legend, the reader is referred to the web version of this article.)

above are shifted along the Burgers vector $\frac{1}{2}[\bar{1}10]$ ($a \rightarrow c$ and $c \rightarrow e$ in Fig. 7). The points a, b, c, d and e correspond to the stable (metastable) positions of GSFE curve described later.

Fig. 8 shows the unit cell of austenite $L1_2$ Fe_3Ga with the slip plane (111) (shaded violet) and slip direction $[\bar{1}\bar{1}2]$ (red arrow). The lattice parameter a is calculated as 3.66 \AA shown in Table 1, which is in a good agreement with experiments [37]. We note that in the $L1_2$ unit cell, Fe atoms remain at six face centers and Ga atoms occupy corners, and thus the atom ratio is still 3:1.

The slip energy barriers (unstable stacking fault energies) and planar defect energies (CSF and APB) are all characterized by the GSFE curve, which is calculated when one half crystal is shifted relative to the other in the slip plane along the slip direction [39]. The $\frac{1}{6}[\bar{1}\bar{1}2](111)$ case of $L1_2$ Fe_3Ga is illustrated in Fig. 9 showing the configuration of slip in the plane (111) with dislocation $\frac{1}{6}[\bar{1}\bar{1}2]$. Fig. 9a is the perfect $L1_2$ lattice before shear, while Fig. 9b is the

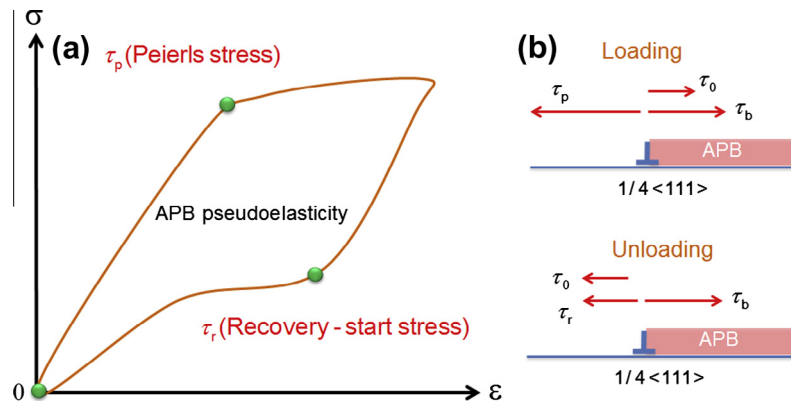


Fig. 6. (a) Schematic illustration of a stress–strain curve shows τ_p (Peierls stress) and τ_r (recovery-start stress) resulting in the APB pseudoelasticity. The τ_p and τ_r have the same sign (both of them are tensile or compressive stresses). (b) Stresses (τ_p, τ_b, τ_0 and τ_r) acting on superpartials during loading and unloading. The τ_b (back stress) pulls back the $\frac{1}{4}[111]$ superpartial due to the APB surface tension; the τ_0 (lattice frictional stress) prohibits the movement of the $\frac{1}{4}[111]$ superpartial.

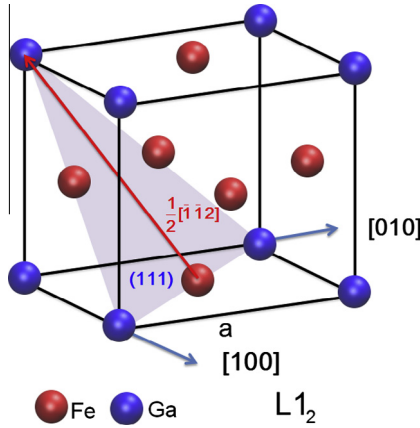


Fig. 8. Slip plane (111) (shaded violet) and slip direction $\frac{1}{2}[\bar{1}\bar{1}2]$ (red arrow) in $L1_2$ Fe_3Ga . In the unit cell, Fe atoms remain at six face centers and Ga atoms occupy corners. (For interpretation of the references to colour in this figure legend, the reader is referred to the web version of this article.)

lattice after shear by one Burgers vector, $u = \frac{1}{6}[\bar{1}\bar{1}2]$ (1.49 Å), in the slip plane. All fault energies can be computed as a function of shear displacement u and are determined relative to the energy of the undeformed $L1_2$.

The calculated GSFE curve in the slip system $\frac{1}{6}\langle 112 \rangle(111)$ is shown in Fig. 10. The points a, b, c, d and e correspond to the stable (metastable) positions in the GSFE curve (see atomic configuration in Fig. 7). The calculated CSF and APB energies are 183 mJ/m^2 and 358 mJ/m^2 , and the calculated unstable stacking fault energies γ_{us1} and γ_{us2} are 512 mJ/m^2 and 941 mJ/m^2 , respectively. We note that these unstable stacking fault energies are significantly high, which will require high applied stress to move these superpartials, and hence the dislocation slip of $L1_2$ Fe_3Ga would require very high stress magnitudes to be activated.

Similar to the dislocation slip in DO_3 , after establishing GSFE curve we also calculated the stresses (τ_p, τ_b, τ_0 and τ_r) acting on superpartials of $L1_2$ during loading and unloading process. The results are shown in Table 2 in the next section.

3. Discussion of the results

We established GSFE curves for dislocation slip in DO_3 and $L1_2$ Fe_3Ga , and calculated slip stresses during loading and unloading processes. The unstable energy barriers for slip in $L1_2$ is much higher than the corresponding levels in DO_3 . Thus, the dislocation

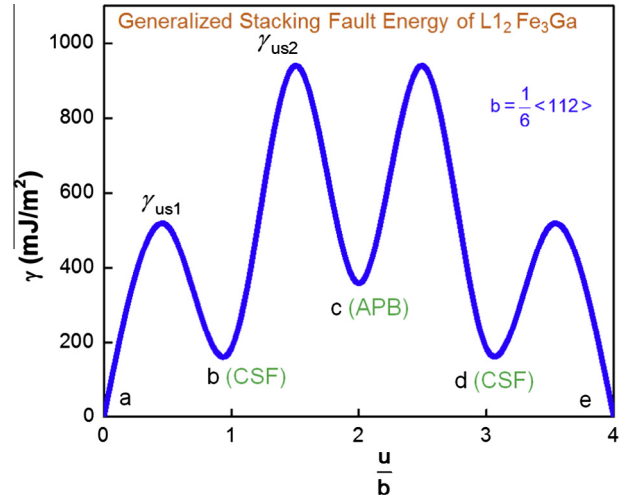


Fig. 10. The GSFE curve of the slip system $\frac{1}{6}\langle 112 \rangle(111)$ in $L1_2$ Fe_3Ga . Upon shearing in the $\langle 112 \rangle$ direction, the dislocation $\frac{1}{6}[110]$ can dissociate into four superpartials $\frac{1}{6}\langle 112 \rangle$ connected by stacking fault energies CSF (183 mJ/m^2) and APB (358 mJ/m^2). The calculated unstable stacking fault energies γ_{us1} and γ_{us2} are 512 mJ/m^2 and 941 mJ/m^2 , respectively. The points a, b, c, d and e correspond to the stable (metastable) positions in the GSFE curve (see atomic configuration in Fig. 7).

Table 2

Calculated stress values (τ_p, τ_b, τ_0 and τ_r) and shear modulus of dislocation slip in DO_3 and $L1_2$ Fe_3Ga . The stresses of DO_3 result in APB pseudoelasticity and are compared with available experimental data [21].

| Structures | Shear stress (MPa) | | | | Shear modulus (GPa) |
|-------------------------|--------------------|----------|----------|----------|---------------------|
| | τ_p | τ_r | τ_b | τ_0 | |
| DO_3 (Present theory) | 320 | 164 | 242 | 78 | 16 |
| DO_3 (Experiments) | 281 | 169 | 225 | 56 | |
| $L1_2$ (Present theory) | 3580 | -900 | 1340 | 2240 | 100 |

slip in $L1_2$ would require very high applied stress magnitudes to be activated in Fe_3Ga . This statement is also confirmed from the calculated Peierls stresses, τ_p , for these two structures shown in Table 2. We note that τ_p is 3580 MPa for slip in $L1_2$, which is much larger than τ_p of 320 MPa in DO_3 . Additionally, we note that the recovery-start shear stress, τ_r , has the same sense with τ_p (both are tensile or compressive) in DO_3 , which results in APB pseudoelasticity and giant recoverable strain. In contrast, these two stresses have different sense (one is tensile and another is compressive)

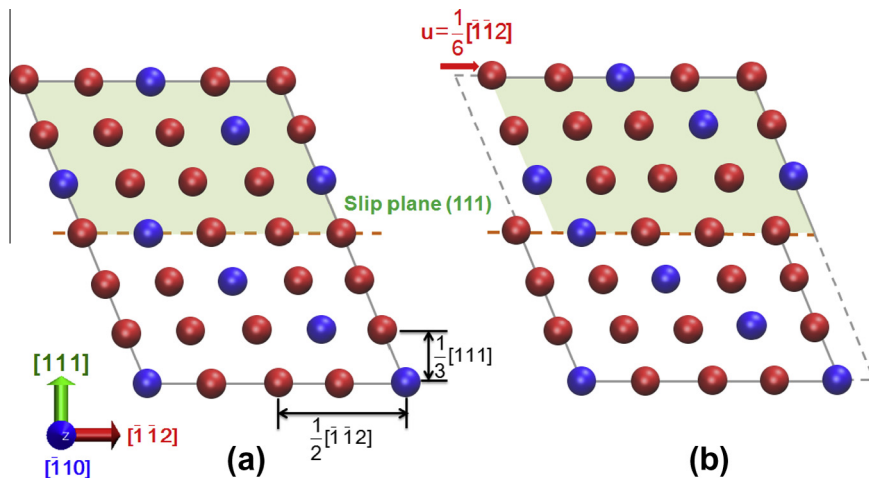


Fig. 9. Dislocation slip in the (111) plane with dislocation $\frac{1}{6}[\bar{1}\bar{1}2]$ of $L1_2$ Fe_3Ga . (a) The perfect $L1_2$ lattice observed from the $[\bar{1}10]$ direction. The slip plane (111) is marked with a brown dashed line. (b) The lattice after a rigid shear with dislocation $\frac{1}{6}[\bar{1}\bar{1}2]$, u , shown in a red arrow. (For interpretation of the references to colour in this figure legend, the reader is referred to the web version of this article.)

in $L1_2$ due to the fact that the back stress, τ_b , is smaller than the lattice frictional stress, τ_0 . In this case, τ_b is not large enough to produce dislocation slip reversion and the sense of the applied stress needs to be reversed during unloading to recover the strain. Therefore, APB pseudoelasticity is not possible in the $L1_2$ structure, and the existence of $L1_2$ will suppress the slip reversibility of DO_3 Fe_3Ga . In Table 2, we also note that the calculated shear modulus of DO_3 is 16 GPa, which is much smaller than 100 GPa of $L1_2$ structure.

The predicted stresses of APB pseudoelasticity in DO_3 lattice shown in Table 2 are in a good agreement with available experimental data. We note that the back stress τ_b and lattice frictional stress τ_0 during the APB pseudoelasticity vary with the annealing time in Fe–Ga alloys, which is associated with the variation in degree of DO_3 order [27]. Furthermore, various experimental treatments can also cause the difference between the predicted values and experimental data. Considering that there could also be other sources of internal stresses due to defects in these alloys the agreement between experiment and theory in Table 2 is considered to be very good.

The distinguishing features of the reversed slip mechanism observed in the iron–gallium alloys compared to slip in other metals are the following: There are limited number of slip systems in the Fe_3Ga case. For the $(111)(110)$ case there are number of independent slip systems. The lack of slip systems produces shuttling of dislocations without interference from dislocations on other planes. Interestingly, the shear stresses are not small in magnitude and the internal back stresses produced are also rather high. The reversibility in metals can be facilitated when dislocation shuttling occurs between precipitates, but the reversible strains are small, often less than 1%. In the case of Fe_3Ga , the reversible strains are

large of the order of 4% which could be exploited further. It should be noted that the same class of iron–gallium alloys exhibit reversible deformations under pseudotwinning conditions – a form of martensitic transformation. Sometimes detwinning of martensite can produce reversibility in shape memory alloys as well. This level of reversibility in iron–gallium is very unique and could produce superior fatigue resistance compared to other metals because fatigue crack initiation and crack advance are direct consequence of irreversible plastic strains. If irreversibility is decreased the plastic strain accumulation leading to fatigue would be reduced.

In summary, we have made advances towards a quantitative understanding of the APB pseudoelasticity in DO_3 Fe_3Ga by precisely establishing the GSFE curves to predict the stresses during loading and unloading. We also calculated the stresses for $L1_2$ Fe_3Ga , and found that the APB pseudoelasticity cannot appear in $L1_2$ lattice since its back stress is not large enough to pull back superpartials. The existence of $L1_2$ will suppress the pseudoelasticity of DO_3 Fe_3Ga , which results in decreasing the strain recovery.

Acknowledgement

The support of National Science Foundation, NSF CMMI 13-00285 is gratefully acknowledged.

Appendix A. Determination of superpartials separation distance

The separations, d_1 and d_2 , of partial dislocations can be calculated using the force balance between attraction due to fault energies and elastic repulsion of partial dislocations [42,43]:

$$\sum F = F_{\text{attraction}}(\gamma) - F_{\text{repulsion}}(K, d) = 0 \quad (A1)$$

This leads to the following equations:

$$\gamma_{\text{NNN}} = K \left\{ \frac{1}{d_1} + \frac{1}{d_1 + d_2} + \frac{1}{2d_1 + d_2} \right\} \quad (A2)$$

$$\gamma_{\text{NNN}} - \gamma_{\text{NN}} = K \left\{ \frac{1}{d_2} + \frac{1}{d_1 + d_2} - \frac{1}{d_1} \right\} \quad (A3)$$

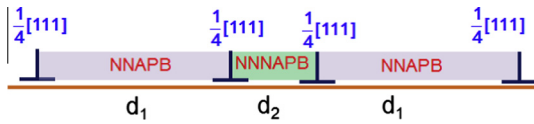


Fig. A1. Separations of partial dislocations for the superdislocation $[111]$.

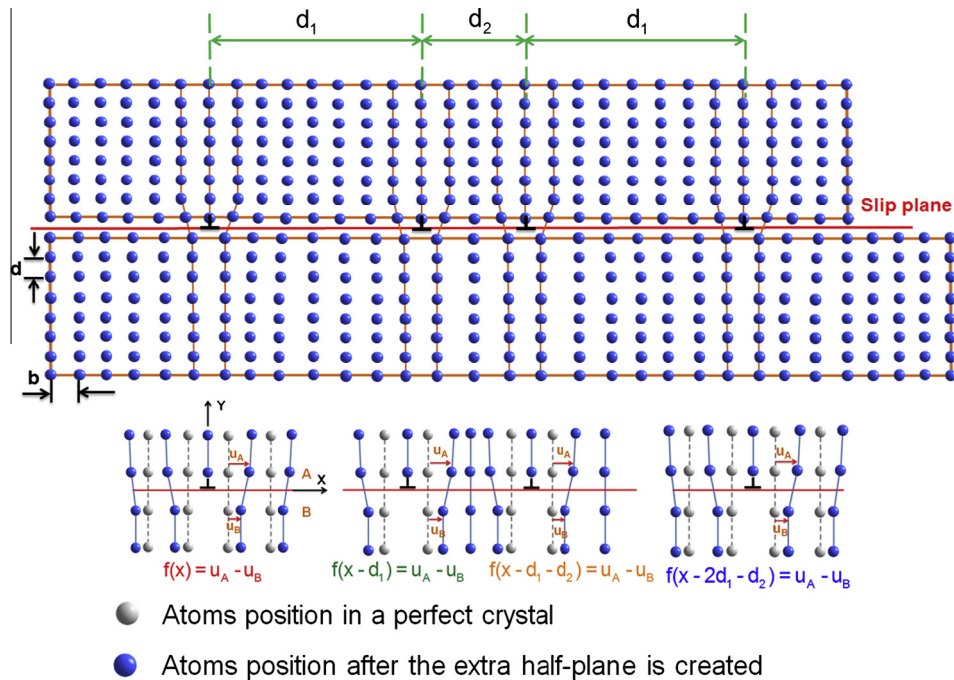


Fig. B1. Schematic of the extended Peierls–Nabarro model involving four superpartials separated by d_1 and d_2 .

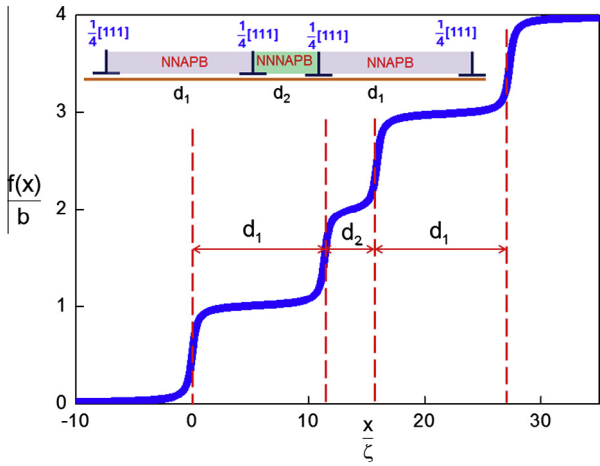


Fig. B2. The disregistry function $f(x)$ for the superdislocation $[111]$ dissociated into four partials $\frac{1}{4}[111]$. The separation distances of the partial dislocations are indicated by d_1 and d_2 .

with γ and K representing the attraction and elastic repulsion force, respectively. These equations can be solved for the separation distances giving the energy levels and the other material constants as input. As noted earlier, $\gamma_{NN} = 34 \text{ mJ/m}^2$ and $\gamma_{NNN} = 71 \text{ mJ/m}^2$. The factor K is given as $K = \frac{\mu b^2}{2\pi}$, where $\mu = 11 \text{ GPa}$ (obtained from our simulations), $b = 2.52 \text{ \AA}$. This results in $d_1 = 5.8 \text{ nm}$ and $d_2 = 2.2 \text{ nm}$ shown in Fig. A1.

Appendix B. Extended Peierls–Nabarro model

To calculate the Peierls stress τ_p , a potential energy of displacement associated with the dislocation movement, misfit energy E_γ , was determined [57,58]. This energy depends on the position of the dislocation line within a lattice cell and reflects the lattice periodicity, thus it is periodic [59–61]. The E_γ is defined as the sum of misfit energies between pairs of atomic planes and is calculated from the GSFE at the local disregistry [33]:

$$E_\gamma = \sum_{m=-\infty}^{+\infty} \gamma[f(ma' - u)]a' \quad (\text{B1})$$

where $\gamma[f(x)]$ is determined from GSFE curve, a' is the periodicity of E_γ and defined as the shortest distance between two equivalent atomic rows in the direction of the dislocation displacement, $f(x)$ is the disregistry function representing the relative displacement of the two half crystals in the slip plane along the x direction [62–64] and u is the position of dislocation line. Fig. B1 is a schematic showing the extended Peierls–Nabarro model involving four superpartials separated by d_1 and d_2 .

The disregistry function $f(x)$ can be described in Eq. (B2) by considering the multiple partials. Fig. B2 shows the normalized $\frac{f(x)}{b}$ variation with $\frac{x}{\zeta}$, where ζ is the half width of the dislocation core.

$$f(x) = \frac{b}{\pi} \left[\arctan\left(\frac{x}{\zeta}\right) + \arctan\left(\frac{x-d_1}{\zeta}\right) + \arctan\left(\frac{x-(d_1+d_2)}{\zeta}\right) + \arctan\left(\frac{x-(2d_1+d_2)}{\zeta}\right) \right] + 2b \quad (\text{B2})$$

After determining the $f(x)$ and approximating the GSFE curve in Fig. 5 by a sinusoidal series function, we can calculate the misfit energy in Eq. (B1). Fig. B3 shows the misfit energy $E_\gamma(u)$ variation with the lattice period a' . Two quantities $(E_\gamma)_{a'/2}$ and $(E_\gamma)_p$ in the plot are denoted. The $(E_\gamma)_{a'/2}$ represents the minimum of $E_\gamma(u)$ function and provides an estimate of the core energy of dislocations.

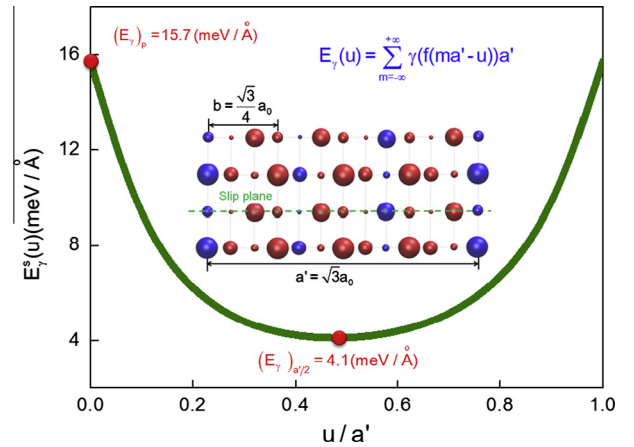


Fig. B3. Misfit energy $E_\gamma(u)$ for the superdislocation $[111]$ of $\text{D0}_3 \text{ Fe}_3\text{Ga}$.

The $(E_\gamma)_p$ is defined as the Peierls energy, which is the amplitude of the variation of $E_\gamma(u)$ and the barrier required to move dislocations [60,65].

References

- [1] T. Duerig, K.N. Melton, D. Stockel, C.M. Wayman, *Engineering Aspect of Shape Memory Alloys*, first ed., Butterworth-Heinemann, UK, 1990.
- [2] L. Delaey, R.V. Krishnan, H. Tas, H. Warlimont, *J. Mater. Sci.* 9 (1974) 1521–1535.
- [3] K. Otsuka, H. Sakamoto, K. Shimizu, *Acta Metall.* 27 (1979) 585–601.
- [4] S. Miyazaki, K. Otsuka, Y. Suzuki, *Scr. Metall.* 15 (1981) 287–292.
- [5] Y. Liu, S.P. Galvin, *Acta Mater.* 45 (1997) 4431–4439.
- [6] E. Hornbogen, *Phys. Status Solidi B* 172 (1992) 161–172.
- [7] E. Patoor, A. Eberhardt, M. Berveiller, *J. Phys.* 5 (1995) 2.
- [8] M. Huang, L.C. Brinson, *J. Mech. Phys. Solids* 46 (1998) 1379.
- [9] J.G. Boyd, D.C. Lagoudas, *Int. J. Plast.* 12 (1996) 805–842.
- [10] Q.P. Sun, K.C. Hwang, *J. Mech. Phys. Solids* 41 (1993) 1.
- [11] K. Gall, H. Sehitoglu, *Int. J. Plast.* 15 (1999) 69.
- [12] K. Otsuka, X. Ren, *Prog. Mater. Sci.* 50 (2005) 511.
- [13] H. Sehitoglu, R. Hamilton, D. Canadinc, X.Y. Zhang, K. Gall, I. Karaman, Y. Chumlyakov, H.J. Maier, *Metall. Mater. Trans. A* 34 (2003) 5–13.
- [14] H.Y. Yasuda, Y. Umakoshi, *MRS Proc.* 1295 (2011) 21–32.
- [15] H.Y. Yasuda, M. Aoki, Y. Oda, K. Fukushima, Y. Umakoshi, in: *International Conference on Advanced Structural and Functional Materials Design*, 10–12 November 2008, IOP Publishing Ltd., UK, 2009, pp. 012053 (012056 pp.).
- [16] L.P. Kubin, A. Fourdeux, J.Y. Guedou, *J. Rieu, Philos. Mag.* A 46 (1982) 357–378.
- [17] H. Yasuda, K. Nakano, T. Nakajima, M. Ueda, Y. Umakoshi, *Acta Mater.* 51 (2003) 5101–5112.
- [18] H.Y. Yasuda, K. Nakano, M. Ueda, Y. Umakoshi, *Trans. Tech. Publ.* (2003) 1801–1806.
- [19] E. Langmaack, E. Nembach, *Philos. Mag. A* 79 (1999) 2359–2377.
- [20] H.Y. Yasuda, M. Aoki, K. Fukushima, Y. Umakoshi, *MRS Proc.* 980 (2007) 315–320.
- [21] H. Yasuda, M. Aoki, A. Takaoka, Y. Umakoshi, *Scr. Mater.* 53 (2005) 253–257.
- [22] Y. Umakoshi, H.Y. Yasuda, T. Nakajima, K. Nakano, K. Yamaoka, M. Ueda, *Acta Mater.* 53 (2005) 5343–5351.
- [23] Y. Umakoshi, T. Nakajima, *Mater. Res. Soc.* (2007) 33–38.
- [24] H.Y. Yasuda, Y. Oda, M. Aoki, K. Fukushima, Y. Umakoshi, *Intermetallics* 16 (2008) 1298–1304.
- [25] H.Y. Yasuda, K. Fukushima, M. Aoki, Y. Umakoshi, *ISIJ Int.* 48 (2008) 1014–1019.
- [26] H. Yasuda, T. Nakajima, Y. Umakoshi, *Intermetallics* 15 (2007) 819–823.
- [27] H.Y. Yasuda, M. Aoki, Y. Umakoshi, *Acta Mater.* 55 (2007) 2407–2415.
- [28] H. Sehitoglu, J. Wang, H.J. Maier, *Int. J. Plast.* 39 (2012) 61–74.
- [29] G. Kresse, J. Furthmuller, *Phys. Rev. B: Condens. Matter.* 54 (1996) 11169.
- [30] G. Kresse, J. Hafner, *Phys. Rev. B: Condens. Matter.* 48 (1993) 13115–13118.
- [31] C.L. Fu, M.H. Yoo, *Acta Metall.* 40 (1992) 703–711.
- [32] V. Paidar, *Czech J. Phys.* 26 (1976) 865–874.
- [33] Y.-M. Juan, E. Kaxiras, *Philos. Mag. A* 74 (1996) 1367–1384.
- [34] J. Wang, H. Sehitoglu, H.J. Maier, *Int. J. Plast.* (2013) (in press).
- [35] N. Srisukhumbowornchai, S. Guruswamy, *J. Appl. Phys.* 92 (2002) 5371–5379.
- [36] N. Srisukhumbowornchai, S. Guruswamy, *J. Appl. Phys.* 90 (2001) 5680–5688.
- [37] T. Suzuki, Y. Oya, S. Ochiai, *Metall. Trans. A* 15 (1984) 173–181.
- [38] V. Vitek, *Phil. Mag.* 18 (1968) 773.
- [39] T. Ezaz, H. Sehitoglu, H.J. Maier, *Acta Mater.* 59 (2011) 5893–5904.
- [40] H. Wang, Y. Zhang, T. Yang, Z. Zhang, L. Sun, R. Wu, *Appl. Phys. Lett.* 97 (2010) 262503–262505.

- [41] Z. Xiao-Xi, L. Jing-Hua, J. Cheng-Bao, *Chin. Phys. Lett.* 27 (2010) 067504.
- [42] A.N. Stroh, *Phil. Mag.* 3 (1958) 625–646.
- [43] R.C. Crawford, I.L.F. Ray, D.J.H. Cockayne, *Phil. Mag.* 27 (1973) 1–7.
- [44] C.E. Feltner, *Phil. Mag.* 12 (1965) 1229–1248.
- [45] J. Friedel, L. Vassamillet, *Dislocations*, Pergamon Press, Oxford, 1964.
- [46] P. Lazar, D.R. Naturarum, *Ab Initio Modelling of Mechanical and Elastic Properties of Solids*, University of Vienna, Vienna, 2006.
- [47] O. Ikeda, R. Kainuma, I. Ohnuma, K. Fukamichi, K. Ishida, *J. Alloys Compd.* 347 (2002) 198–205.
- [48] H.-X. Xie, L. Bo, T. Yu, *Phil. Mag.* 92 (2012) 1542–1553.
- [49] O.N. Mryasov, Y.N. Gornostyrev, M. van Schilfgaard, A.J. Freeman, *Acta Mater.* 50 (2002) 4545–4554.
- [50] G. Schoeck, S. Kohlhammer, M. Fahnle, *Philos. Mag. Lett.* 79 (1999) 849–857.
- [51] R. Voskoboinikov, C. Rae, *IOP Conference Series: Materials Science and Engineering*, IOP Publishing, 2009, p. 012009.
- [52] Y. Sun, G.E. Beltz, J.R. Rice, *Mater. Sci. Eng., A* 170 (1993) 67–85.
- [53] K. Suzuki, M. Ichihara, S. Takeuchi, *Acta Metall.* 27 (1979) 193–200.
- [54] B.L. Lü, G.Q. Chen, S. Qu, H. Su, W.L. Zhou, *Mater. Sci. Eng., A* 565 (2013) 317–320.
- [55] P. Müllner, A. King, *Acta Mater.* 58 (2010) 5242–5261.
- [56] A.E. Romanov, A.L. Kolesnikova, *Prog. Mater. Sci.* 54 (2009) 740–769.
- [57] E.B. Tadmor, R.E. Miller, *Modeling Materials: Continuum Atomistic and Multiscale Techniques*, Cambridge University Press, 2011.
- [58] F.R.N. Nabarro, *Proc. Phys. Soc.* 59 (1947).
- [59] G. Schoeck, *Phys. Rev. Lett.* 82 (1999) 2310–2313.
- [60] B. Joós, Q. Ren, M.S. Duesbery, *Phys. Rev. B* 50 (1994) 5890–5898.
- [61] S. Ogata, L. Ju, S. Yip, *Phys. Rev. B: Condens. Matter Mater. Phys.* 71 (2005) 224102.
- [62] P. Carrez, D. Ferré, P. Cordier, *Phil. Mag.* 87 (2007) 3229–3247.
- [63] L. Lejček, *Czech J. Phys.* 23 (1973) 176–178.
- [64] B. Joós, M.S. Duesbery, *Phys. Rev. Lett.* 78 (1997) 266–269.
- [65] A.E. Romanov, *Eur. J. Mech. A. Solids* 22 (2003) 727–741.